4 Remote sensing of snow albedo, grain size, and pollution from space

Alexander A. Khokanovsky
Institute of Environmental Physics, University of Bremen, Germany

Summary

Snow reflectance in the visible region of the electromagnetic spectrum depends on the amount and type of pollutants. Fresh and clean snow is very reflective and its albedo is close to one, almost irrespective of grain size. On the other hand, snow with larger grains is less reflective in the near-infrared, compared with finely grained snow. This is due to the enhanced light absorption by large ice grains compared with the small ones. This difference in reflectance can be actually measured, and it provides a means of determining the grain effective radius and, therefore, the separation of different types of snow (e.g., snow with very fine, fine, medium, coarse, very coarse, and extreme grains (see, e.g., the classification http://www.crrel.usace.army.mil/library/booksnongovernment/Seasonal_Snow.pdf).

The size of snow grains is important for determining snow albedo, snow thickness using microwave techniques, the thermal environment within the snowpack and, also, for detecting signs of snow melt and snowfall. In this chapter we have summarized the techniques used for estimating snow grain size, snow albedo and level of pollution, using spaceborne observations. The main focus of the chapter is on the theoretical background of snow grain size and albedo/pollution monitoring using spaceborne observations. The presented results can be also used for the interpretation of optical airborne and ground-based observations of snowfields and the cryosphere in general.

4.1 Introduction

Optical remote sensing techniques are used for the determination of various snow parameters, including the concentration of pollutants in snow, the average ice grain size and the snow spectral albedo (Dozier and Painter, 2004). The extent of global snow cover and its temporal behavior can be also studied using optical remote sensing methods (Seidel and Martinec (2004); see Chapter 3 of this book). Generally,

Remote Sensing of the Cryosphere, First Edition. Edited by M. Tedesco.

Companion Website: www.wiley.com/go/tedesco/cryosphere

fresh snow is a very bright object in the visible range. However, the brightness decreases considerably if snow is contaminated by soot, dust or algae (Warren, 1982). The decrease in snow brightness can be easily detected by a radiometer or spectrometer operated in the UV-visible spectral range (see Table 4.1).

The snow reflectance is hardly influenced by the grain size in the UV-visible region of the electromagnetic spectrum. However, ice grains absorb solar light in the near-IR spectral range and the amount of absorbed electromagnetic energy depends on the grain size being larger for larger grains. This reduces light reflectance in the near-IR spectral range (e.g., at the wavelength 1.24 μm) and can be also easily detected using optical measurements.

As a matter of fact, snow darkening is proportional to the square root of the snow grain size in the visible (Kokhanovsky *et al.*, 2011). Both snow grain size and the amount of impurities determine snow spectral albedo, which can be easily calculated using radiative transfer theory for the defined levels of snow pollution and snow grain size (see, for example, the online calculator at http://snow.engin.umich.edu/). The focus of this chapter is on the theoretical background of snow grain size and albedo/pollution monitoring using spaceborne observations. The presented results can be also used for the interpretation of optical airborne and ground-based observations of snow fields and the cryosphere in general.

There are several approaches to retrieve the grain size from the spectral reflectance of snow in the near-infrared region of the electromagnetic spectrum (Bourdelles and Fily, 1993; Fily *et al.*, 1997; Green *et al.*, 2002; Scambos *et al.*, 2007; Stamnes *et al.*, 2007; Zege *et al.*, 2011; Kokhanovsky and Rozanov, 2012). The processing software is based either on the look-up-tables calculated using the exact solution of radiative transfer equation (Stamnes *et al.*, 2007) or the asymptotic radiative transfer theory (Kokhanovsky and Rozanov, 2012). In particular, the spectral reflectance measurements at the wavelengths 0.46 and 0.865 μm were used by Stamnes *et al.* (2007) for the retrieval of snow impurity concentration and grain size. The subsurface snow grain size was retrieved using measurements at 1.6 μm.

It should be pointed out that snow has a layered structure (Colbeck, 1991), with different grain sizes along different layers. Therefore, the retrieved particle size depends on the channel used, because of different penetration depths occurring at different wavelengths. This enables a profiling of snow grain size using spectral reflectance measurements (Li *et al.*, 2001). Kokhanovsky *et al.* (2011) used the asymptotic radiative transfer theory and measurements at 0.44 and 0.865 μm for the retrieval of snow grain size. Lyapustin *et al.* (2009) used the same theory, except the band ratio (0.645 and 1.24 μm) was used. Zege *et al.* (2011) used the MODIS measurements at the wavelengths 0.47, 0.86, and 1.24 μm.

The use of multiple channels (or their ratio) offers the possibility of improving the accuracy of the algorithm (at least for vertically homogeneous snow layers). Nolin and Dozier (2000) proposed a hyperspectral method for the determination of snow grain size. They used the snow spectral reflectance centered at 1.03 μm, the wavelength of a prominent ice absorption feature. The interpretation is based on the area – not the depth – of the absorption feature scaled to absolute reflectance. Therefore, the method does not require topographic correction and is insensitive to the instrument noise.

Table 4.1 Channels of relevant remote sensing instruments (new channels as compared to heritage instruments are given in bold) used for snow remote sensing. Airborne and ground-based instrumentation is described by Dozier and Painter (2004), Green *et al.* (2006), and Aoki *et al.* (2007).

Instrument	Channels	Comments
MODIS	0.4125, 0.443, 0.469, 0.488, 0.531, 0.551, 0.555, 0.645, 0.667, 0.678, 0.748, 0.858, 0.8695, 0.905, 0.936, 0.940, 1.24, 1.375, 1.64, 2.13, 3.75, 3.959, 4.05, 4.465, 4.516, 6.715, 7.325, 8.55, 9.73, 11.03, 12.02, 13.335, 13.635, 13.935, 14.235 μm	Bandwidth: 10–50 nm ($\lambda \leq 2.2$ μm Spatial resolution: 0.25 –1 km Swath: 2330 km
MISR	0.446, 0.558, 0.672, 0.866 μm	Bandwidth: 20–40 nm Spatial resolution: 0.275 km Swath: 360 km Viewing zenith angles (for the same target): 0, 26.1, 45.6, 60, 70.5 degrees in forward backward views
MERIS, 01.03.2002–08.04.2012	0.4125, 0.4425, 0.49, 0.51, 0.56, 0.62, 0.665, 0.68125, 0.705, 0.75375, 0.76, 0.775, 0.865, 0.89, 0.9 μm	Bandwidth: 7.5–20 nm (3.75 nm at $\lambda = 760.625$ nm) Spatial resolution: 0.3 km Swath: 1150 km
SeaWiFS, 18.09.1997–11.12.2010	0.412, 0.443, 0.49, 0.51, 0.555, 0.67, 0.765, 0.865 μm	Bandwidth: 20 nm Spatial resolution: 1.1 km Swath: 2801 km
SEVIRI	0.635, 0.81, 1.64, 3.92, 6.25, 7.35, 8.7, 9.66, 10.8, 12, 13.4 μm	Bandwidth: 15–30 nm ($\lambda \leq 1.64$ μm) Spatial resolution: 0.25–1.0 km for most of channels Geostationary (15 min repetition time from 0° longitude)
GLI, 14.12.02–24.10.2003	0.38, 0.4, 0.412, 0.443, 0.46, 0.49, 0.52, 0.545, 0.565, 0.625, 0.666, 0.68, 0.678, 0.71, 0.749, 0.763, 0.825, 0.865, 1.05, 1.135, 1.24, 1.38, 1.64, 2.21, 3.715, 6.7, 7.3, 8.6, 10.8, 12 μm	Bandwidth: 10 nm ($\lambda \leq 0.865$ μm) Spatial resolution: 3.0 km for most of channels Swath: 1600 km
MSI (S-2) 2015 ESA, Europe	0.443, 0.490, 0.560, 0.665, 0.705, 0.740, 0.775, 0.842, 0.865, 0.940, 1. 375, 1.61, 2.19 μm	13 bands 4 bands – 10 m 6 bands – 20 m 3 bands – 60 m Bandwidth: 20–115 nm Swath: 290 km
OLCI (S-3) 2015 ESA, Europe	0.400, 0.412, 0.443, 0.490, 0.510, 0.560, 0.620, 0.665, **0.67375**, 0.68125, 0.70875, 0.75375, 0.76125, **0.76435**, **0.7675**, 0.77875, 0.865, 0.885, 0.900, **0.94**, **1.02** μm	21 bands All bands – 300 m Bandwidth: 2.5–40nm Swath: 1300 km (5 cameras)
SLSTR (S-3) 2015 ESA, Europe	0.555, 0.659, 0.865, **1.375**, 1.61, **2.25**, 3.74, 10.95, 12.0 μm	9 bands (**dual view**) 6 bands – 500 m 3 bands – 1000 m (TIR) Bandwidth: 15–60 nm (0.38–1 μm in TIR) Swath: 1700 km (750 km for backward view)

Table 4.1 (*continued*)

Instrument	Channels	Comments
MSI (Earthcare) 2016 ESA-JAXA, Europe-Japan	0.659, 0.865, 1.61, 2.2, 8.8, 10.8, 12 μm	Bandwidth: 0.02, 0.02, 0.06, 0.1, 0.9, 0.9, 0.9 μm, respectively Spatial resolution: 500 m Swath: 150 km
VIIRS (NPP) 2011 NASA, USA	0.412, 0. 445, 0.488, 0.555, 0.64, 0.672, 0.7, 0.746, 0.865, 1.24, 1.378, 1.61, 2.25, 3.7, 4.05, 8.55, 10.673, 11.45, 12.013 μm	Bandwidth: 15–60 nm (0.18–1.0 μm in TIR) Spatial resolution: 400–800 m Swath: 3000 km
S-GLI 2016 JAXA, Japan	0.38, 0.412, 0.443, 0.490, 0.530, 0.565, 0.670, 0.763, 0.865, 1.05, 1.38, 1.64, 2.21, 10.8, 12.0 μm	Bandwidth: 10–20 nm (0.05–0.7 μm in TIR) Spatial resolution: 250–1000 m Swath: 1400 km, channels 0.67 and 0.865 μm will also provide information on polarization characteristics of reflected light and perform multi-angular observations

The method was applied to the data of Airborne Visible/Infrared Imaging Spectrometer (AVIRIS). Painter *et al.* (2003) developed a method for the retrieval of sub-pixel snow grain size also using AVIRIS. The measured AVIRIS spectral reflectance was matched with the theoretical one, iterating the grain size and snow cover for a ground scene under study. Green *et al.* (2002) used AVIRIS data to map the solid, liquid, and vapor phases of water in snow analyzing spectral reflectance at 0.94, 0.98, and 1.03 μm, and using the fact that the absorption feature in reflectance moves to somewhat longer wavelengths while going from the vapor to the crystalline state of the same matter.

4.2 Forward modeling

The optical instrument measures the specific intensity I of the reflected, transmitted or internal light field. A recent review on the directional radiometry, the notion of the specific intensity, and radiative transfer is given by Mishchenko (2011). In satellite applications, the reflection function:

$$R(\mu_0, \mu, \varphi) = I^{\uparrow}(\mu_0, \mu, \varphi)/I_L^{\uparrow}(\mu_0) \tag{4.1}$$

is used. Here, $I^{\uparrow}(\mu_0, \mu, \varphi)$ is the specific intensity of reflected light for a given target, $I_L^{\uparrow}(\mu_0)$ is the specific intensity of reflected light for a perfectly reflecting Lambertian white screen (with albedo 1.0), μ_0 is the cosine of the solar zenith angle (SZA), μ is the cosine of the viewing zenith angle (VZA), and φ is the difference of the solar and observations azimuthal angles.

The relative azimuth angle is equal to zero in the glint region (SZA = VZA) and is equal to π in the exact backscattering direction. The value of $I_L^{\uparrow}(\mu_0)$ can be easily calculated if the irradiance of the incident solar radiation E_0 on an area perpendicular to the light beam is known (Liou, 2002; Kokhanovsky, 2006):

$$I_L^{\uparrow}(\mu_0) = \mu_0 E_0/\pi \tag{4.2}$$

Both E_0 and $I^{\uparrow}(\mu_0, \mu, \varphi)$ can be measured by sensors mounted on satellites. This enables the calculation of the reflection function:

$$R(\mu_0, \mu, \varphi) = \pi I^{\uparrow}(\mu_0, \mu, \varphi)/\mu_0 E_0 \tag{4.3}$$

or of the bidirectional reflectance distribution function, BRDF $= R/\pi$.

It follows that, to retrieve snow properties from optical satellite data, it is important to provide some means for the calculation of the reflection function for different observation geometries. This is usually done in the framework of the radiative transfer theory (Chandrasekhar, 1960; Liou, 2002). In particular, one needs to specify the boundary conditions, the spectral single scattering albedo ω_0, the optical thickness τ and phase function $p(\theta)$ (θ is the scattering angle) for a given turbid medium (e.g., snow, ice), and solve the radiative transfer equation for the specific intensity of reflected light. In most cases, snow can be considered as a semi-infinite medium. Then only parameters ω_0 and $p(\theta)$ must be specified if the effects of vertical snow inhomogeneity are ignored. Advanced snow radiative transfer models account for the vertical variation of snow single scattering albedo, phase function, and extinction coefficient.

The radiative transfer equation is usually solved numerically. However, in the case of weakly absorbing media such as snow, the approximate solution of the radiative transfer equation is possible. In particular, the reflection function (for a vertically homogeneous snow) can be presented as (Zege *et al.*, 1991; Kokhanovsky, 2006):

$$R(\mu_0, \mu, \varphi) = R(\mu_0, \mu, \varphi)A^n, A = \exp[-\alpha], \quad n = K_0(\mu_0)K_0(\mu)/R_0(\mu_0, \mu, \varphi) \tag{4.4}$$

where $R_0(\mu_0, \mu, \varphi)$ is the reflection function of a semi-infinite non-absorbing snow layer, A is the spherical albedo of snow, and

$$\alpha = 4\sqrt{\frac{\beta}{3(1-g)}}, \qquad K_0(\mu) = \frac{3}{7}(1+2\mu) \tag{4.5}$$

Here, $\beta = 1 - \omega_0$ is the probability of photon absorption in a unit volume of snow, g is the asymmetry parameter, $K_0(\mu)$ is the so-called escape function (van de Hulst, 1980). Kokhanovsky (2006) proposed the following parameterization for $R_0(\mu_0, \mu, \varphi)$:

$$R_0(\mu_0, \mu, \varphi) = \frac{a + b(\mu_0 + \mu) + c\mu_0\mu + p(\theta)}{4(\mu_0 + \mu)} \tag{4.6}$$

$$p(\theta) = 11.1 \exp(-0.087\theta) + 1.1 \exp(-0.014\theta) \tag{4.7}$$

$$\cos\theta = -\mu_0\mu + \sqrt{(1-\mu_0^2)(1-\mu^2)}\cos\varphi, \qquad a = 1.247, \quad b = 1.186, \quad c = 5.157 \tag{4.8}$$

Here θ is the scattering angle in degrees.

This parameterization was performed on the assumption that the snow particles can be presented as rough fractal ice crystals. The results for rough hexagonal particles produce similar phase functions (see Figure 4.1).

In the case of a two-layered snow model, the following approximation can be used:

$$R_0(\mu_0, \mu, \varphi) = R(\mu_0, \mu, \varphi, \tau) + \frac{At^2 K_0(\mu_0) K_0(\mu)}{1 - Ar} \tag{4.9}$$

where:

$R(\mu_0, \mu, \varphi, \tau)$ is the reflection function of the upper layer (for the case of an underlying black surface)

A is the spherical albedo of the second layer.

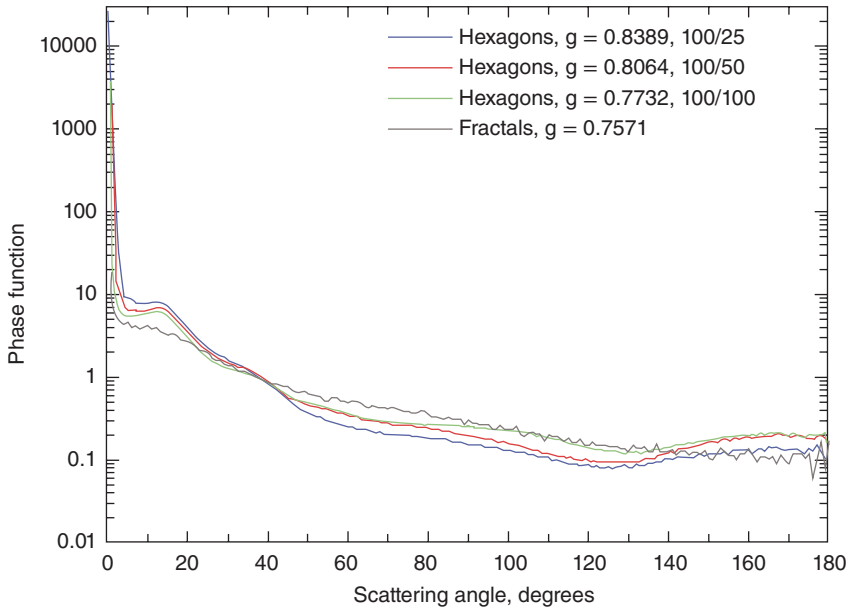

Figure 4.1 The dependence of the phase function on the shape of particles. The following shapes were considered: hexagons with the length to the diameter ratios equal to 100/25, 100/50, 100/100 μm and fractal particles (Macke *et al.*, 1996) at wavelength 550 nm. The diameter is defined as the distance between opposite sides of the hexagon. For all particles, the surface was assumed to be rough in the calculations (Khokanovsky 2011. Reproduced with permission of Taylor & Francis).

The functions $R(\mu_0, \mu, \varphi, \tau)$, $r(\tau)$ and $t(\tau)$ for the upper layer can be calculated either using the radiative transfer equation solution or an approximation (Zege *et al.*, 1991; Kokhanovsky, 2006):

$$R(\mu_0, \mu, \varphi, \tau) = R_0(\mu_0, \mu, \varphi, \tau)\exp(-\alpha n) - t\exp(-x-\alpha)K_0(\mu_0)K_0(\mu),$$
$$t(\tau) = \frac{\sinh\alpha}{\sinh(\varepsilon x+\alpha)}, r(\tau) = \exp(-\alpha) - t(\tau)\exp(-x-\alpha), \quad (4.10)$$
$$\varepsilon = 1.072, x = \gamma\tau, \alpha = 4q\gamma, q = \frac{1}{3(1-g)}, \gamma = \sqrt{3\beta(1-g)}$$

Here, local optical parameters (e.g., β, g) correspond to that of an upper snow layer. The case of arbitrary number of layers was considered by Kokhanovsky (2006). Equation 4.9 is often used also in the case of a single snow layer deposited on the surface (e.g., grass) with the spherical albedo A. The equations given above can be used to estimate the snow spectral single scattering albedo (or the parameter β) from spectral snow reflectance measurements for an assumed phase function (and, therefore, value of g) of a snow layer (see Figure 4.1). Look-up-tables based on the exact radiative transfer equation solution can be also used (Stamnes *et al.*, 2007). The determination of the snow grain size and level of pollution requires the derivation of the relationships between local optical and microphysical snow characteristics. This is discussed in the next section.

4.3 Local optical properties of a snow layer

We will assume that snow consists of ice grains and other scatterers (e.g., soot, dust, algae, etc.) suspended in air. The dense media effects (Tsang *et al.*, 2000) are ignored. Then the snow extinction coefficient k_{ext}, absorption coefficient k_{abs}, and phase function $p(\theta)$ can be presented as:

$$k_{ext} = k_{ext}^{ice} + \sum_{j=1}^{N} k_{ext,j} \quad (4.11)$$

$$k_{abs} = k_{abs}^{ice} + \sum_{j=1}^{N} k_{abs,j} \quad (4.12)$$

$$p(\theta) = \frac{k_{sca}p^{ice}(\theta) + \sum_{j=1}^{N} k_{sca,j}p_j(\theta)}{k_{sca} + \sum_{j=1}^{N} k_{sca,j}} \quad (4.13)$$

Here, "ice" means that the parameter corresponds to the pure snow (no impurities, only ice phase), $k_{sca} = k_{ext} - k_{abs}$ is the scattering coefficient, and the account for N impurities is given in the second terms of corresponding expressions. The probability of photon absorption is calculated as $\beta = k_{abs}/k_{ext}$ and the asymmetry

parameter $g = \frac{1}{2}\int_0^{\pi} p(\theta)\sin\theta\cos\theta d\theta$. All local optical characteristics given above can be computed using Mie theory for spherical particles (Mie, 1908) or geometrical optics approaches (van de Hulst, 1981; Liou, 2002; Kokhanovsky, 2006) for particles of different shapes. Also, approximations, look-up-tables, and parameterizations of results of exact calculations are possible. The selected approximations are discussed below.

The extinction and absorption coefficients of the pure ice can be presented as:

$$k_{ext}^{ice} = NC_{ext}, k_{abs}^{ice} = NC_{abs} \tag{4.14}$$

where:

C_{ext} and C_{abs} are average extinction and absorption cross-sections of snow grains
$N = c_i/V$ is the number concentration of snow grains (c_i is their volumetric concentration and V is the average volume of grains).

In the framework of the geometrical optics approximation, it follows that (Kokhanovsky, 2006):

$$C_{ext} = 2\Sigma, C_{abs} = \xi\gamma V \tag{4.15}$$

for large (as compared to the wavelength), randomly oriented ice grains of arbitrary shape. The expression for C_{abs} presented here is valid in the case of weakly absorbing large particles such as ice grains in the visible and near IR regions of the electromagnetic spectrum (Kokhanovsky and Zege, 2004). Here, Σ is the average projection area of the particles and $\gamma = \frac{4\pi\kappa_i(\lambda)}{\lambda}$, κ_i is the imaginary part of the ice refractive index at the wavelength λ. The parameter ξ depends on the shape of particles (being close to 1.28 for ice spheres; Kokhanovsky and Zege, 2004) and the real part of the ice refractive index. Its dependence on the size of particles can be ignored in the visible and near-IR regions of the electromagnetic spectrum. Let us introduce the effective grain size (EGS) as:

$$a_{ef} = \frac{3V}{4\Sigma} \tag{4.16}$$

The value of a_{ef} coincides with the radius of particles in the case of monodispersed spheres. Then one easily derives for the probability of photon absorption:

$$\beta = \sigma\gamma a_{ef} \tag{4.17}$$

where $\sigma = 2\xi/3$ ($\approx$0.85 for spheres) (Kokhanovsky and Zege, 2004).

The phase function of ice grains depends on the assumed shapes of scatterers. It is often assumed that snow grains can be presented as fractal particles (Macke *et al.*, 1996). The corresponding phase function does not differ considerably from the phase function measured *in situ* in ice clouds (Kokhanovsky *et al.*, 2011). The asymmetry parameter for this phase function is equal approximately to 0.76 in the visible (see Figure 4.1).

The parameter α (see Equation 4.5) in the case of pure snow(no pollutants) is as follows:

$$\alpha = \sqrt{\gamma a_{ef}}\mathbf{P} \tag{4.18}$$

where $\mathbf{P} = 4\sqrt{\sigma/3(1-g)}$. The parameter α and, therefore, the grain size a_{ef}, can be derived from snow reflectance measurements, assuming the shape of particles.

In particular, the shape of particles determines the value of $\mathbf{P}$. The geometric optics calculations for spherical particles give $\mathbf{P} = 6.3$. It is difficult to calculate this parameter from first principles, due to the irregular shape of snow grains. Therefore, it is important to report both values $\mathbf{P}$ and a_{ef} in outputs of corresponding retrieval algorithms. One can also introduce the optically equivalent radius $\alpha_{opt} = \mathbf{P}^2 a_{ef}$. This radius can be directly derived from the reflectance measurements and is less influenced by assumptions on the shape of particles. It can be also used to find the spectral snow albedo using a simple approximation:

$$A(\lambda) = \exp\left\{-\sqrt{\gamma(\lambda)\,\alpha_{opt}}\right\} \tag{4.19}$$

Let us consider the polluted snow now. If we assume that soot is the only pollutant, then we may assume that light scattering and extinction in snow is dominated by ice grains. The equation for the parameter β must be modified as:

$$\beta = \beta_{ice} + \beta_{soot} \tag{4.20}$$

It follows (see Equation 4.17) that:

$$\beta_{ice} = \sigma\gamma a_{ef} \tag{4.21}$$

Let us introduce the soot mass absorption coefficient ε:

$$k_{abs}^{soot} = \varepsilon\rho_s c_s \tag{4.22}$$

where ρ_s is the soot density and c_s is the volumetric concentration of snow grains.

Taking into account that $k_{ext} = 1.5c_i/a_{ef}$ (Kokhanovsky, 2006), one derives:

$$\beta_s = \frac{2c_s}{3c_i}\varepsilon\rho_s a_{ef} \tag{4.23}$$

We will assume that $\varepsilon : \lambda^{-1}$ (as for Rayleigh scatterers) and, therefore, $\varepsilon(\lambda) = \varepsilon(\lambda_0)\lambda_0/\lambda$. Taking into account the formulae given above, we arrive to the following equation:

$$\alpha(\lambda) = \sqrt{(B_i\chi_i(\lambda) + B_s c)x_{ef}} \tag{4.24}$$

where:

$$B_i = \frac{32\sigma}{3(1-g)},\quad B_s = \frac{16\rho_i\varepsilon(\lambda_0)\lambda_0}{9\pi(1-g)},\quad c = \frac{\rho_s c_s}{\rho_i c_i},\quad x_{ef} = \frac{2\pi a_{ef}}{\lambda} \tag{4.25}$$

and $\rho_i = 0.9167$ g/cm^3 is the ice density.

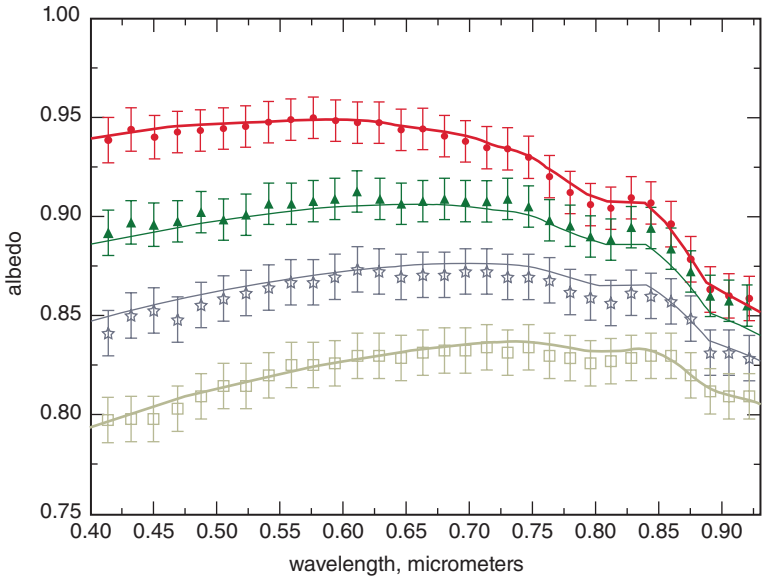

Figure 4.2 Measured spectral dependence of plane albedo (Hadley and Kirchstetter, 2012) at the nadir illumination and various levels of soot absorption (soot concentrations are 1.1e-7(filled circles), 4.5e-7(triangles), 8.6e-7(stars), 1.68e-6 (boxes)). The effective radius of particles is 55 microns. The results of calculations are given by the solid lines. The imaginary part of ice refractive index was taken from Warren and Brandt (2008).

The function $\alpha(\lambda)$ given in Equation 4.24 can be used to find the snow spherical albedo $A(\lambda) = \exp(-\alpha(\lambda))$, the plane albedo $A_p = A^{K_0(\mu_0)}$ and also the snow BRDF, as discussed above.

A comparison of calculations according to these equations with experimental results for the plane albedo is given in Figure 4.2. The excellent agreement of theory with the experiment performed by Hadley and Kirchstetter (2012) is found, assuming that $B_i = 77.02$, $B_s = 22.15$. These parameters were derived using the minimization procedure at the largest concentration of pollutants (see Figure 4.2). Theoretical calculations for spherical particles give $\xi = 1.28$, $g = 0.884$ (Kokhanovsky and Zege, 2004) and $B_i = 78.47$. It follows that theoretical and experimental values of B_i are in a good agreement. The theoretical value of B_s cannot be derived, because the value of $\epsilon(\lambda_0)$ for soot in snow was not determined experimentally. The experimental value of $B_s = 22.15$ is consistent with the assumption that $\epsilon(0.435\ \mu m) = 9.27\ g/cm^3$ (see Equation 4.25), which is plausible for the laboratory experiment performed by Hadley and Kirchstetter (2012).

4.4 Inverse problem

The soot concentration and snow grain size are usually found using two approaches: 1) look up table (LUT) and 2) asymptotic theory. In the case of the LUT approach (Stamnes *et al.*, 2007), the radiances are pre-calculated at several channels and then the parameters a_{ef} and c are sought, by minimizing the difference of observed and calculated spectra of light reflected from the snow.

The asymptotic theory enables the analytical inversion. Therefore it is described in more detail here for the case of dual-channel retrievals:

$$R_1 = R_0 \exp\left[-\sqrt{\left(B_i\chi_{i,1} + B_s c\right) x_{ef}}\right], \qquad R_2 = R_0 \exp\left[-\sqrt{\left(B_i\chi_{i,2} + B_s c\right) x_{ef}}\right] \tag{4.26}$$

The value of a_{ef} from the second equation in 4.26 (the measurements in the near IR) can be represented via R_2 and c. Namely, it follows that:

$$a_{ef} = \frac{\ln^2(R_2/R_0)}{\kappa(B_i\chi_{i,2} + B_s c)} \tag{4.27}$$

where $\kappa = 2\pi/\lambda$. The corresponding equation is substituted to the first equation in 4.26. This enables the determination of c as:

$$c = \frac{\Psi_1 - \Xi\Psi_2}{(\Xi - 1)B_s} \tag{4.28}$$

where $\Psi_1 = \mathrm{B_i}\chi_{\mathrm{i1}}, \Psi_2 = \mathrm{B_i}\chi_{\mathrm{i2}}$, $\Xi = \ln^2(R_1/R_0)/\ln^2(R_2/R_0)$. The effective radius is then found from Equation 4.27. In principle, the measurements at several channels can be used simultaneously. This enables, for example, the illumination of constant R_0 in Equation 4.28 (Zege *et al.*, 2011). One should avoid the application of the algorithm to directions close to the forward (glint) and backward scattering geometries, and also to cases with a low Sun (with SZA $< 75°$), where the accuracy of the underlying theory drops (Kokhanovsky and Breon, 2012; Wiebe *et al.*, 2013).

The application of the algorithm described above to the MEdium Resolution Imaging Spectrometer (MERIS) data is shown in Figure 4.3 (Kokhanovsky *et al.*, 2011). Currently, there are several algorithms based on the asymptotic theory (Tedesco and Kokhanovsky, 2007, 2010; Lyapustin *et al.*, 2009; Zege *et al.*, 2011; Wiebe *et al.*, 2013). The principal differences between them are discussed by Kokhanovsky and Rozanov (2012).

An example of retrievals based on the LUT approach over Arctic from Global Imager (GLI) data is shown in Figure 4.4 (Hori *et al.*, 2007). The retrievals based on the asymptotic radiative transfer theory for the Moderate-resolution Imaging Spectroradiometer (MODIS) data are shown in Figure 4.5 (Lyapustin *et al.*, 2009). In particular, the results presented in Figure 4.5 quantify the temporal change of snow grain size over Greenland (for the time period April to August, 2004).

The soot concentration in snow is generally very small and, therefore, the accuracy of retrievals of the parameter c is low (Aoki *et al.*, 2007; Zege *et al.*, 2011; Warren, 2013). The dependence of the spherical albedo A on soot concentration is given in Figure 4.6.

Assuming combined measurement and forward modeling errors around 5%, we arrive at the conclusion that the retrievals of concentrations of soot below 50 – 100 ng/g are hardly possible from a satellite. Zege *et al.* (2011) have also reached this conclusion, suggesting the use of their method for remote sensing of

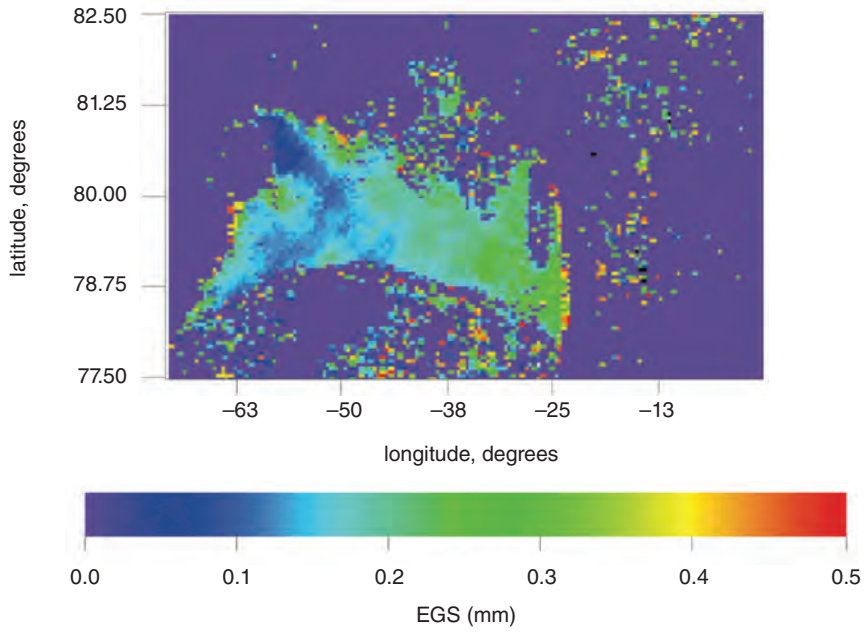

Figure 4.3 The snow effective radius derived from MERIS observations (Khokanovsky 2011. Reproduced with permission of Taylor & Francis).

soot only at high levels of snow pollution (above 1000 ng/g). On the other hand, the concentration of soot in the Arctic is usually in the range 3–30 ng/g (Warren, 2013). Values are even lower in Antarctica. Therefore, spaceborne retrievals are possible only close to rural areas and also for occasional pollution events. Therefore, we confirm the findings of Warren (2013) that optical remote sensing is not likely to be useful for quantifying the effect of black carbon on snow albedo (except for areas with a high concentration of pollutants).

However, the temporal changes of snow albedo (without attribution to specific causes) can be well determined from a satellite. In particular, Strove *et al.* (2005) have found that the mean difference between the MODIS algorithm albedo retrievals and the *in situ* data is less than 0.02 for all the stations in Greenland combined (RMSE = 0.07). Thus, the corresponding retrievals can be used not only for climate modeling but also for ice sheet mass balance studies.

Snow albedo can be easily calculated at any wavelength if the values of a_{ef} and c are retrieved. It is possible to retrieve the snow albedo directly from the reflectance (see Equation 4.4): $A = (R/R_0)^{1/n}$; the albedo derived in such a way is less influenced by *a priori* assumptions. Models of the bidirectional reflectance of snow, created using a discrete ordinate radiative transfer model, can be also used for the retrievals of snow albedo, as demonstrated by Klein and Stroeve (2002) and Stroeve *et al.* (2005).

The validation of snow grain size, snow albedo and concentration of impurities retrievals has been performed by Nolin and Dozier (2000), Stroeve *et al.* (2005), Aoki *et al.* (2007), Kokhanovsky *et al.* (2011), and Wiebe *et al.* (2013). The error

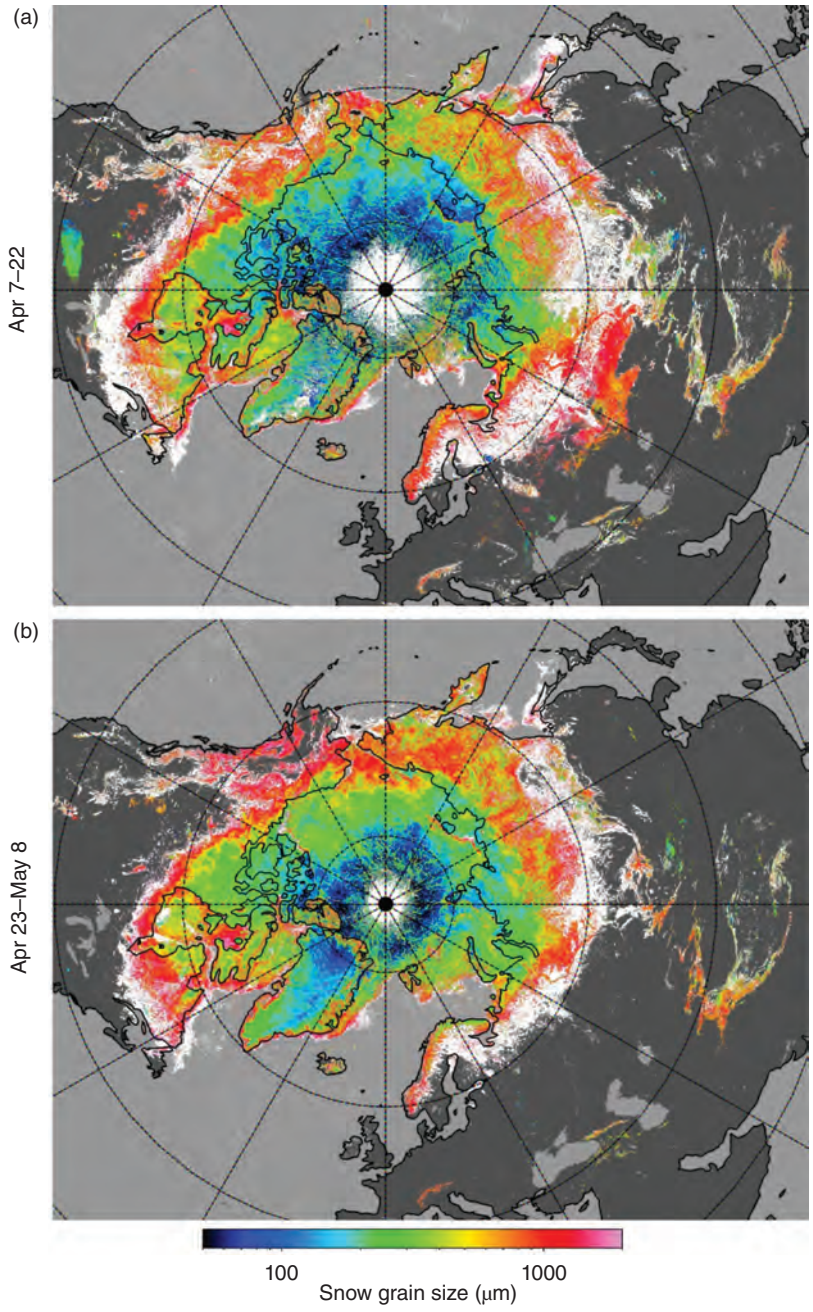

Figure 4.4 The retrieved snow grain size (16-day average, April 7 to May 8, 2003) based on the LUT approach (Hori *et al.*, 2007. Reproduced with permission of Elsevier).

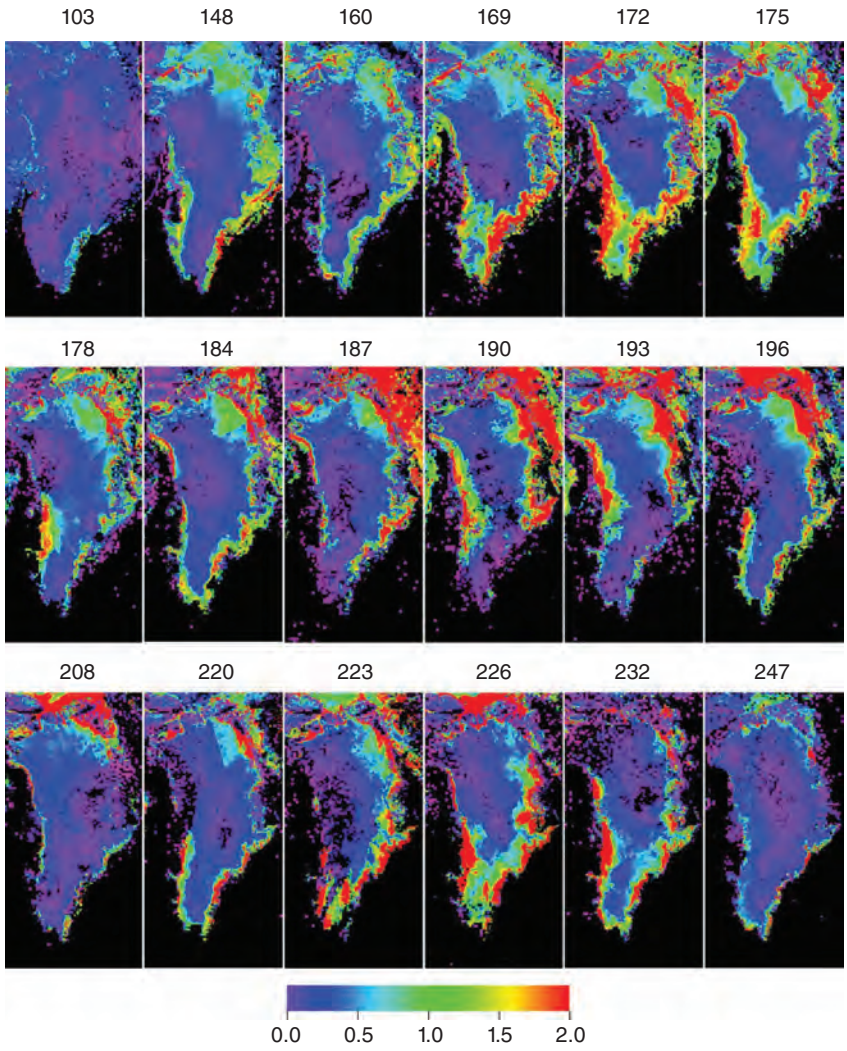

Figure 4.5 Snow grain size (mm) retrieved from MODIS TERRA data for the melting period of 2004 (April – August). Each image is obtained as a three-day composite to cover gaps caused by clouds. The numbers give a Julian day (Lyapustin *et al.*, 2009. Reproduced with permission of Elsevier).

on snow albedo is on average within 0.02, as stated above. The value of a_{ef} is difficult to measure on the ground (also in view of its spatial variability within a pixel), although a high correlation between the ground – measured and satellite – retrieved grain sizes has been found (Aoki *et al.*, 2007). Because of the lack of standard methods to measure the snow grain size on the ground, results depend on the experience of the observer and the selection of the grain size definition (largest or the smallest crystal size, etc.).

The results of the validation campaign for the satellite determination of soot concentration performed by Aoki *et al.* (2007) show that the coefficients of correlation between *in situ* and satellite-derived values of c are considerably lower (0.36 – 0.51), compared to the results for a_{ef} as derived from optical measurements

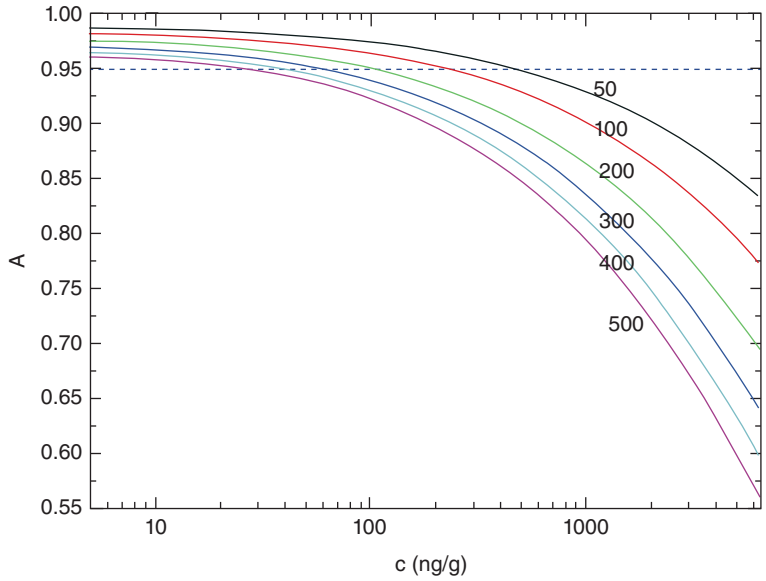

Figure 4.6 The dependence of spherical albedo on the soot concentration for various effective radii of snow grains (50, 100, 200, 300, 400, and 500 μm).

at the wavelength 0.9 μm (0.82). This is most probably due to the fact that the snow was contaminated not only by soot but also by other impurities (e.g., dust), with high mass concentrations in the range 70 – 60 000 ng/g.

4.5 Pitfalls of retrievals

The retrievals as described above look quite simple. However, there are complications due to atmospheric effects and, also, due to assumptions on the snow field properties under study (e.g., horizontally and vertically inhomogeneous snow layers, finite snow depth and influence of underlying surface, wet snow, snow on the slopes of mountains, snow in forested areas, blowing snow, slash, firn, etc.). Selected problems related to optical remote sensing of snow from space are discussed in this section.

Cloud screening is difficult over snow. Clouds look similar to snow if viewed from a satellite. Therefore, robust cloud screening algorithms (over snow) are needed ahead of retrievals. Cloud screening over snow is usually performed using the following:

a) the analysis of reflectance in gaseous absorption bands (oxygen A-band, water vapor, etc);
b) different time scales for snow and cloud variability (accumulation of images, reference image);
c) the analysis of differential Snow Index (the 865/885 nm ratio contrast is lower for cloudy scenes);

d) the study of the shape of spectral reflectance curves (UV-VIS-NIR);
e) the analysis of brightness temperature differences at the wavelengths 3.7, 10.8, and 12 μm.

Atmospheric correction is performed, either assuming the standard polar atmosphere model (Stamnes *et al.*, 2007) or deriving the aerosol properties (e.g., aerosol optical thickness over snow) using spectral or multi-angular spaceborne observations (Istomina *et al.*, 2011; Mei *et al.*, 2012).

In the case of Lambertian underlying surfaces, the signal as detected on a satellite can be represented as follows:

$$R(\mu_0, \mu, \varphi) = R_{atm}(\mu_0, \mu, \varphi, \tau) + \frac{A_{surf} T}{1 - A_{surf} r} \tag{4.29}$$

where:

T is the total atmospheric transmittance from a satellite to the snowfield and back
A_{surf} is the surface albedo to be found
r is the spherical albedo of atmosphere
$R_{atm}(\mu_0, \mu, \varphi, \tau_{aer})$ is the atmospheric path reflectance.

It follows from this equation:

$$A_{surf} = \frac{R_{mes}(\mu_0, \mu, \varphi) - R_{atm}(\mu_0, \mu, \varphi, \tau)}{(R_{mes}(\mu_0, \mu, \varphi) - R_{atm}(\mu_0, \mu, \varphi, \tau))r + T} \tag{4.30}$$

This equation can be used to find the surface albedo (and also snow grain size) under the assumption of the Lambertian ground. Zege *et al.* (2011) proposed a way to account for the effects of non-Lambertian underlying surfaces.

The vertical snow inhomogeneity can impact the quality of retrievals. Snow has a layered structure (Colbeck, 1991). Therefore, complications occur when several wavelengths are used to retrieve the snow grain size. The penetration depth of solar light in snow is different for different wavelengths; therefore, the assumption that the grain size is the same if multiple wavelengths are used is violated. This introduces a bias in the retrievals for layered snow layers. One way around this problem is to use the two-layered snow model (Li *et al.*, 2001). In particular, it follows:

$$R(\mu_0, \mu, \varphi) = R(\mu_0, \mu, \varphi, \tau) + \frac{A t^2 K_0(\mu_0) K_0(\mu)}{1 - Ar} \tag{4.31}$$

Here r, t are the spherical albedo and transmittance of the upper layer, respectively, $R(\mu_0, \mu, \varphi, \tau)$ is the reflection function of the upper layer (for the case of an underlying black surface), A is the spherical albedo of the second layer. The functions $R(\mu_0, \mu, \varphi, \tau)$, $r(\tau)$ and $t(\tau)$ can be calculated either using the radiative transfer equation solution or an approximation, as described above.

The upper/bottom snow effective radius and upper snow ice water path can be retrieved using Equation 4.31. For this, one needs to fit the observations and calculations at several wavelengths.

Clearly, if the penetration depth of radiation is smaller than the thickness of the upper snow layer, then the properties of the second (buried) snow layer (or layers) cannot be determined. The analysis of Jacobians given in Figure 4.7 (Kokhanovsky *et al.*, 2011) suggests that optical remote sensing gives the sub-surface grain size only (1 – 2 cm from the surface).

The study of snow microstructure at larger depths is hardly possible using optical methods (except when techniques based on optical measurements along vertical snow walls are employed (Nikolaeva and Kokhanovsky, 2012). The same is true for

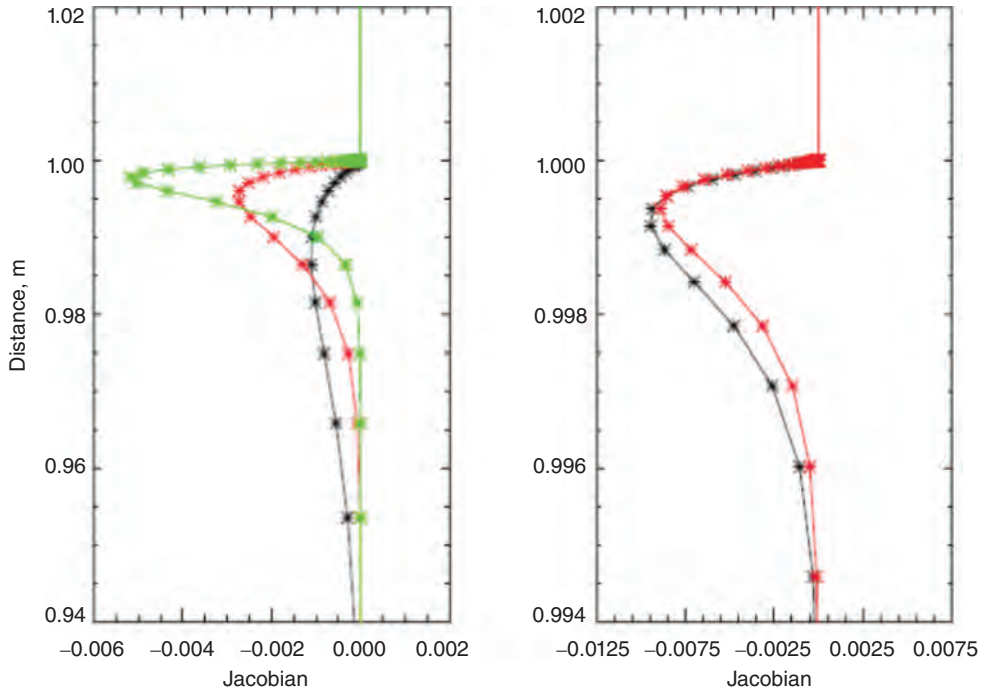

Figure 4.7 Dependence of the Jacobian J_a for effective radius of ice crystals in snow on the distance from the snow bottom at the wavelengths 865 nm (black curve), 1020 nm (red curve), and 1240 nm (green curve) (left panel). Right panel: the same except at the wavelengths 1610 nm (red) and 2190 nm (black). The LOWTRAN aerosol model with the aerosol optical thickness equal to 0.05 was used. The snow geometrical thickness is equal to 1 m and the length of side of fractal particles is equal to 50 μm (first panel), 300 μm (second panel), 750 μm (third panel). The concentration of soot is equal to 10 – 8. The solar zenith angle is equal to 60° and the observation is at the nadir direction (Khokanovsky and Rozanov 2012. Reproduced with permission of Springer).

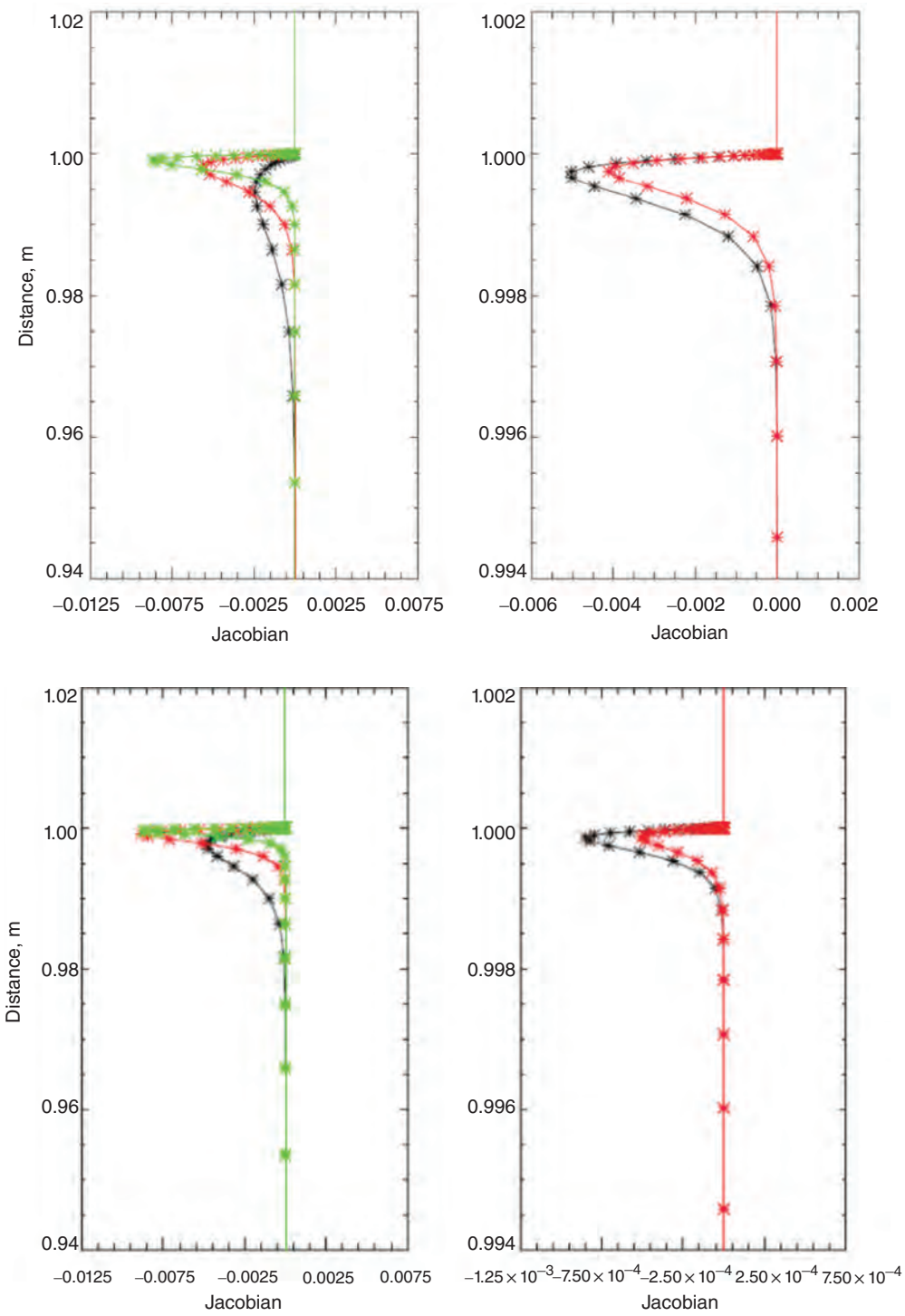

Figure 4.7 (*continued*)

the snow pollution determination. Only pollution in upper snow layer/layers can be studied (up to 10 cm or so – see Figure 4.8).

The snow horizontal inhomogeneity is usually ignored. For retrieval purposes, it is generally assumed that the snow surface is ideally flat and is horizontally homogeneous. However, this is rarely the case, especially if the instrument is located on a satellite and has a poor spatial resolution. Patches of vegetation and forest can be present in the satellite scene (Tedesco and Kokhanovsky, 2007) But, even in the absence of vegetation, the prevailing winds and ice stress can produce horizontal snow inhomogeneities (ridges, sastrugi, see, e.g., the MISR browse imagery presented for the 79° backward viewing camera in Figure 4.9, http://eosweb.larc.nasa.gov/HPDOCS/misr/misr_html/Antarctica_ice_waves.html). This will bias retrievals. In particular, if the solar illumination is perpendicular to sastrugi, then albedo decreases due to the substantial trapping of photons by vertical walls of

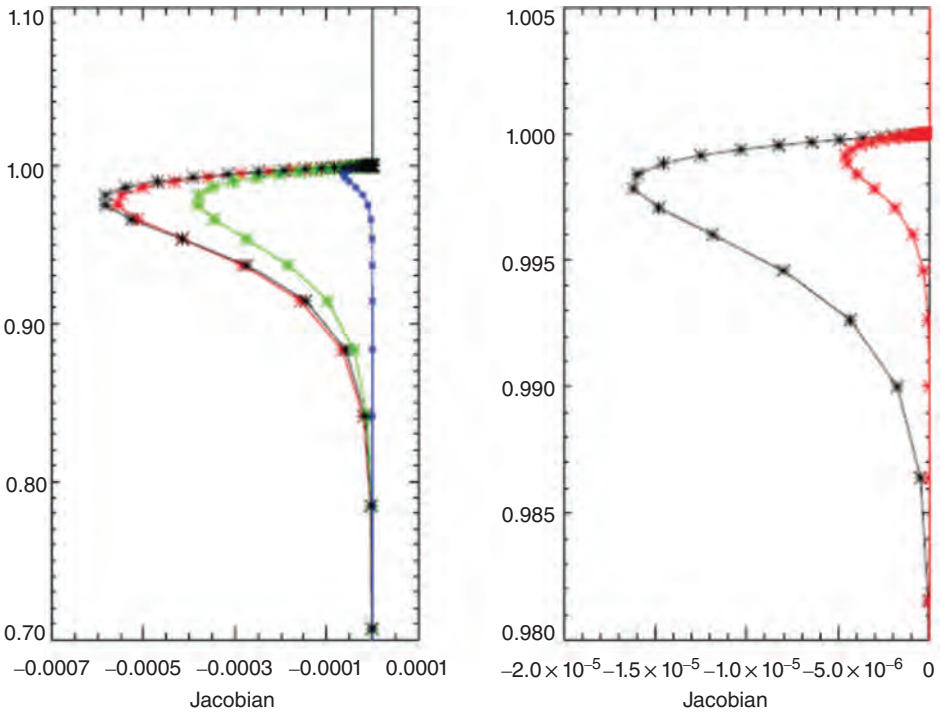

Figure 4.8 Dependence of the Jacobian for soot concentration $J_c(\lambda, z)$ on the distance from the snow bottom at the wavelengths 400, 443, 555, 670 nm (left, larger Jacobians at maximum correspond to a smaller wavelength) and at wavelengths 865 and 1029nm (right, larger Jacobians at maximum correspond to a smaller wavelength). The LOWTRAN aerosol model with the aerosol optical thickness equal to 0.05 was used. The snow geometrical thickness is equal to 1 m and the length of side of fractal particles is equal to 50 μm (first panel), 300 μm (second panel), 750 μm (third panel). The concentration of soot is equal to 10^{-8}. The solar zenith angle is equal to 60° and the observation is at the nadir direction (Khokanovsky and Rozanov 2012. Reproduced with permission of Springer).

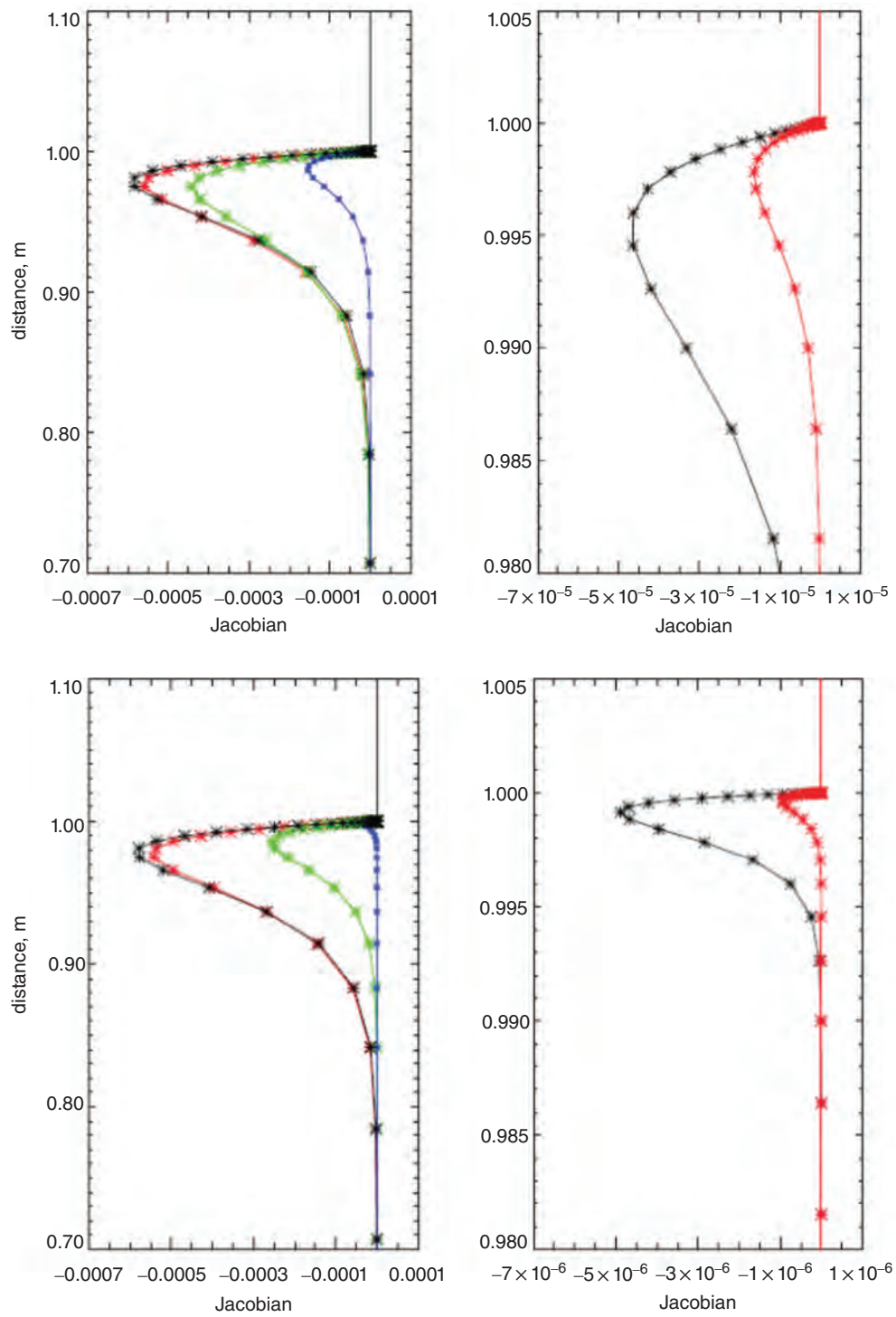

Figure 4.8 (*continued*)

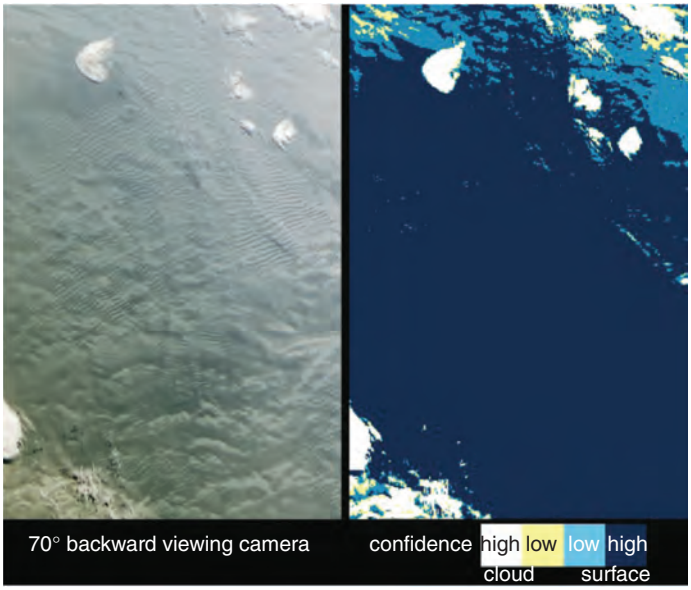

Figure 4.9 The MISR browse image over Antarctica for the 70° backward viewing camera (December 16, 2004; (http://eosweb.larc.nasa.gov/HPDOCS/misr/misr_html/antarctica_ice_waves.html) (NASA).

sastrugi (Kuchiki *et al.*, 2011; Zuravleva and Kokhanovsky, 2011). This decrease in albedo due to purely geometrical effects (up to 30% for the single scattering albedo equal to 0.98; Zuravleva and Kokhanovsky, 2011) can be erroneously interpreted as increase in the grain size (or level of pollution).

4.6 Conclusions

Remote sensing optical data can be used for the determination of subsurface snow properties without disturbing snow. To achieve this aim, the spectral solar light reflectance governed by the snow pollution and snow grain size must be measured in the visible and near-infrared regions. Snow reflectance in the visible region depends on the amount and type of pollutants. Fresh and clean snow is very reflective, and its albedo is close to 1.0, almost irrespective of grain size. On the other hand, snow with larger grains is less reflective in the near infrared, compared to snow with fine grains. This is due to the enhanced light absorption by large ice grains compared with small ones.

This difference in reflectance can be actually measured and provides a means for the determination of the grain effective radius and, therefore, the separation of different types of snow (e.g., snow with very fine ($a^{ef} < 0.1$ mm), fine (0.1 – 0.25 mm), medium (0.25 – 0.5mm), coarse (0.5 – 1.0mm), very coarse (1.0 – 2.5 mm), and extreme (> 2.5 mm) grains (http://www.crrel.usace.army.mil/library/booksnongovernment/Seasonal_Snow.pdf). The size of snow grains is important for determining snow albedo and the thermal environment within the snowpack, and also for detecting of signs of snowmelt and snowfall. In this chapter, we have

summarized some techniques used for estimating snow grain size and albedo and the level of pollution using spaceborne observations. Similar techniques are used for ground- based and airborne optical snow remote sensing.

Acknowledgments

This work was supported by the BMBF Project CLIMSLIP and FP7 Project SIDARUS. It was conducted as part of the GCOM-C/SGLI Snow Project supported by Japan Aerospace Exploration Agency (JAXA). The author is grateful to O.L. Hadley for providing the experimental data (see Figure 4.2) in a tabular form. The author is grateful for a cooperation and discussions on snow grain size retrievals with T. Aoki, G. Heygster, M. Hori, A. Lyapustin, F. Seidel, V.V. Rozanov, M. Tedesco, and E.P. Zege.

References

Aoki, T., Hori, M., Motoyoshi, H., *et al.* (2007). ADEOS-II/GLI snow/ice products – Part II: Validation results using GLI and MODIS data. *Remote Sensing of Environment* **111**, 274–290.

Bourdelles, B. & Fily, M. (1993). Snow grain-size determination from Landsat imagery over Terre Adélie, Antarctica. *Annals of Glaciology* **17**, 86–92.

Chandrasekhar, S. (1960). *Radiative Transfer*. New York: Dover.

Colbeck, S.C. (1991). The layered structure of snow layers. *Reviews of Geophysics* **29**(1), 81–96.

Dozier, J. & Painter, T.H. (2004). Multispectral and hyperspectral remote sensing of alpine snow properties. *Annual Review of Earth and Planetary Sciences* **32**, 465–494.

Fily, M., Bourdelles, B., Dedieu, J.P. & Sergent, C. (1997). Comparison of in situ and Landsat Thematic Mapper derived snow grain characteristics in the Alps. *Remote Sensing of Environment* **59**(3), 452–460.

Green, R.O., Dozier, J., Roberts, D.A. & Painter, T.H. (2002). Spectral snow reflectance models for grain size and liquid water fraction inmelting snow for the solar reflected spectrum. *Annals of Glaciology* **34**, 71–73.

Green, R.O., Painter, T.H., Roberts, D.A. & Dozier, J. (2006). Measuring the expressed abundance of the three phases of water with an imaging spectrometer over melting snow. *Water Resources Research* **42**, W10402. doi:10.1029/2005WR004509.

Hadley, O. & Kirchstetter, W. (2012). Black-carbon reduction of snow albedo. *Nature Climate Change* **2**, 437–440.

Hori, M., Aoki, T., Stamnes, K., Chen, B. & Li, W. (2007). ADEOS-II/GLI snow/ice products – part III: Retrieved results. *Remote Sensing of Environment* **111**, 274–319.

Istomina, L.G., von Hoyningen-Huene, W., Kokhanovsky, A.A., Schultz, E. & Burrows, J.P. (2011). Remote sensing of aerosols over snow using infrared AATSR observations. *Atmospheric Measurement Techniques* **4**, 1133 – 1145.

Klein, A.G. & Stroeve, J. (2002). Development and validation of a snow albedo algorithm for the MODIS instrument. *Annals of Glaciology* **34**, 45 – 52.

Kokhanovsky, A.A. (2006). *Cloud Optics*. Dordrecht: Springer.

Kokhanovsky, A.A. & Breon, F.-M. (2012). Validation of an analytical snow BRDF model using PARASOL multi-angular and multispectral observations. *IEEE Geoscience and Remote Sensing Letters* **5**, 928 – 932.

Kokhanovsky, A.A. & Rozanov, V.V. (2012). The retrieval of snow characteristics from optical measurements. In: Kokhanovsky, A.A. (ed). *Light Scattering Reviews* **6**, 289 – 331.

Kokhanovsky, A.A. & Zege, E.P. (2004). Scattering optics of snow. *Applied Optics* **43**, 1589 – 1602.

Kokhanovsky A.A., Rozanov, V.V., Aoki, T., Odermatt, D., Brockmann, C., Krüger, O., Bouvet, M., Drusch, M. & Hori, M. (2011). Sizing snow grains using backscattered solar light. *International Journal of Remote Sensing* **32**, 6975 – 7008.

Kuchiki, K., Aoki, T., Niwano, M., Motoyoshi, H. & Iwabuchi, H. (2011). Effect of sastrugi on snow bidirectional reflectance and its applications to MODIS data. *Journal of Geophysical Research* **116**. doi: 10.1029/2011JD016070.

Li, W., Stamnes, K., Chen, B. & Xiong, X. (2001). Snow grain size retrieved from near-infrared radiances at multiple wavelengths. *Geophysical Research Letters* **28**, 1699 – 1702.

Liou, K.N. (2002). *An Introduction to Atmospheric Radiation*. New York, NY, Academic Press.

Lyapustin, A., Tedesco, M., Wang, Y., Aoki, T., Hori, M. & Kokhanovsky, A. (2009). Retrieval of snow grain size over Greenland from MODIS. *Remote Sensing of Environment* **113**, 1976 – 1987.

Macke, A., Mueller, J. & Raschke, E. (1996). Scattering properties of atmospheric ice crystals. *Journal of the Atmospheric Sciences* **53**, 2813 – 2825.

Mei, L., Xue, Y., de Leeuw, G., *et al.* (2012). Aerosol optical depth retrieval in the Arctic region using MODIS over snow. *Remote Sensing of Environment* **128**, 234 – 245.

Mie, G. (1908). Beiträge zur Optik trüber Medien, speziell kolloidaler Metallösungen. *Annals of Physics* **330**, 377 – 445.

Mishchenko, M.I. (2011). Directional radiometry and radiative transfer: A new paradigm. *Journal of Quantitative Spectroscopy and Radiative Transfer* **112**, 2079 – 2094.

Nikolaeva, O.V. & Kokhanovsky, A.A. (2012). Theoretical study of solar light reflectances from vertical snow surfaces. *Cryosphere Discussions* 4205 – 4231.

Nolin, A.W. & Dozier, J. (2000). A hyperspectral method for remotely sensing the grain size of snow. *Remote Sensing of Environment* **74**, 207–216.

Painter, T.H., Dozier, J., Roberts, D.A., Davis, R.E. & Green (2003). Retrieval of subpixels snow-covered area and grain size from imaging spectrometer data. *Remote Sensing of Environment* **85**, 64–77.

Scambos, T.A., Haran, T.M., Fahnestock, M.A., Painter, T.H. & Bohlander, J. (2007). MODIS-based mosaic of Antarctica (MOA) data sets: continent-wide surface morphology and snow grain size. *Remote Sensing of Environment* **111**, 242–257.

Seidel, K. & Martinec, J. (2004). *Remote Sensing in Snow Hydrology*. Berlin, Springer-Praxis.

Stamnes, K., Li, W., Eide, H., Aoki, T., Hori, M. & Storvold, R. (2007). ADEOS-II GLI snow/ice products – Part I. Scientific basis. *Remote Sensing of Environment* **111**, 258–273.

Stroeve, J., Box, J.E., Gao, F., Liang, S., Nolin, A. & Schaaf, C. (2005). Accuracy assessment of the MODIS 16-day albedo product for snow: comparisons with Greenland in situ measurements. *Remote Sensing of Environment* **94**, 46–60.

Tedesco, M. & Kokhanovsky, A.A. (2007). The semi-analytical snow retrieval algorithm and its application to MODIS data. *Remote Sensing of Environment* **111**, 228–241.

Tedesco, M. & Kokhanovsky, A.A. (2010). Errata of the paper: "The semi-analytical snow retrieval algorithm and its application to MODIS data". *Remote Sensing of Environment* **115**, 255.

Tsang, L., Chen, C.-T., Chang, A. T. C., Guo, J. & Ding, K.-H. (2000). Dense media radiative transfer theory based on quasicrystalline approximation with applications to passive microwave remote sensing of snow. *Radio Science* **311**, 731–750.

van de Hulst, H.C. (1980). *Multiple Light Scattering*, v.1, 2. New York, NY, Academic Press.

van de Hulst, H.C. (1981). Light Scattering by Small Particles. New York, NY, Dover.

Warren, S.G. (1982). Optical properties of snow. *Reviews of Geophysics and Space Physics* **20**, 67–89.

Warren, S.G. (2013). Can be black carbon in snow be detected by remote sensing? *Journal of Geophysical Research* (in press).

Warren, S.G. & Brandt, R.E. (2008). Optical constants of ice from ultraviolet to the microwave: A revised compilation. *Journal of Geophysical Research* **113**, D14220. doi: 10.1029/2007JD009744.

Wiebe, H., Heygster, G., Zege, E.P., Aoki, T. & Hori, M. (2013). Snow grain size retrieval SGSP from optical satellite data: validation with ground measurements and detection of snowfall events. *Remote Sensing of Environment* **128**, 11–20.

Zege E.P., Katsev, I.L. & Ivanov, A.P. (1991). *Image Transfer through a Scattering Medium*. Heidelberg: Springer.

Zege, E.P., Katsev, I.L., Malinka, A.V., Prikhach, A.S., Heygster, G. & Wiebe, H. (2011). Algorithm for retrieval of the effective snow grain size and pollution amount from satellite measurements. *Remote Sensing of Environment* **115**, 2674 – 2685.

Zuravleva, T.B. & Kokhanovsky, A.A. (2011). Influence of surface roughness on the reflective properties of snow. *Journal of Quantitative Spectroscopy and Radiative Transfer* **112**, 1353 – 1368.

Acronyms

AVIRIS	Airborne Visible/Infrared Imaging Spectrometer
SZA	Solar zenith angle
VZA	Viewing zenith angle
EGS	Effective grain size
LUT	Look up table
MERIS	MEdium Resolution Imaging Spectrometer
GLI	Global Imager
MODIS	Moderate-resolution Imaging Spectroradiometer
MISR	Multi-angle Imaging SpectroRadiometer
JAXA	Japan Aerospace Exploration Agency

Websites cited

http://snow.engin.umich.edu/

http://eosweb.larc.nasa.gov/HPDOCS/misr/misr_html/Antarctica_ice_waves.html

http://www.crrel.usace.army.mil/library/booksnongovernment/Seasonal_Snow.pdf